Falkner-Skan boundary layer approximation in Rayleigh-Bénard convection

Shishkina, O., Horn, S. & Wagner, S.

Original citation & hyperlink:

Shishkina, O, Horn, S & Wagner, S 2013, 'Falkner-Skan boundary layer approximation in Rayleigh-Bénard convection' Journal of Fluid Mechanics, vol. 730, pp. 442-463.
https://dx.doi.org/10.1017/jfm.2013.347

DOI 10.1017/jfm.2013.347
ISSN 0022-1120
ESSN 1469-7645

Publisher: Cambridge University Press

Falkner–Skan boundary layer approximation in Rayleigh–Bénard convection

Olga Shishkina†, Susanne Horn, Sebastian Wagner

DLR - Institute for Aerodynamics and Flow Technology, Bunsenstraße 10, 37073 Göttingen, Germany

(Received 19 February 2013)

To approximate the velocity and temperature within the boundary layers in turbulent thermal convection at moderate Rayleigh numbers, we consider the Falkner–Skan ansatz, which is a generalization of the Prandtl–Blasius one to a non-zero-pressure-gradient case. This ansatz takes into account the influence of the angle of attack β of the large-scale circulation of a fluid inside a convection cell against the heated/cooled horizontal plate. With respect to turbulent Rayleigh–Bénard convection, we derive several theoretical estimates, among them the limiting cases of the temperature profiles for all angles β, for infinite and for infinitesimal Prandtl numbers $\mathcal{P}r$. Dependences on $\mathcal{P}r$ and β of the ratio of the thermal to viscous boundary layers are obtained from the numerical solutions of the boundary layers equations. For particular cases of β, accurate approximations are developed as functions on $\mathcal{P}r$. The theoretical results are corroborated by our direct numerical simulations for $\mathcal{P}r = 0.786$ (air) and $\mathcal{P}r = 4.38$ (water). The angle of attack β is estimated based on the information on the locations within the plane of the large-scale circulation, where the time-averaged wall shear stress vanishes. For the considered fluids it is found that $\beta \approx 0.7\pi$ and the theoretical predictions based on the Falkner–Skan approximation for this β leads to a better agreement with the DNS results, compared to the Prandtl–Blasius approximation for $\beta = \pi$.

Key words: Turbulent Rayleigh–Bénard convection, boundary layer equations, boundary layer thickness, Falkner–Skan equation, Direct Numerical Simulations

1. Introduction

Turbulent thermal convection between two horizontal plates with lower heated and upper cooled flat surfaces, has been the subject of numerous experimental and numerical studies. This problem is known as turbulent Rayleigh–Bénard convection (RBC) and for reviews on it we refer to Siggia (1994); Ahlers *et al.* (2009); Lohse & Xia (2010); Chillà & Schumacher (2012).

In turbulent thermal convection for moderate Rayleigh numbers the thermal boundary layers, which are located close to the heated or cooled horizontal plates, and the viscous boundary layers, which are attached to all rigid walls, can be transitional or even laminar (Ahlers *et al.* 2009). In this case the mean flow characteristics within the boundary layers are usually approximated using the Prandtl–Blasius ansatz, i.e. under the assumption that the wind of turbulence (or Large Scale Circulation – LSC) above the viscous boundary layer is horizontal and constant, which leads to a zero pressure derivative with respect to the wind direction.

† Email address for correspondence: Olga.Shishkina@dlr.de

In contrast to this, recent Direct Numerical Simulations (DNS) of turbulent RBC in different fluids showed that, first, the time-averaged pressure gradient does not vanish (Shi *et al.* 2012); second, the wind is non-constant along its path and, third, the ratio of the thicknesses of the thermal and viscous boundary layers, although being almost constant along the wind, is approximately two times larger than that predicted by the Prandtl–Blasius equations (Wagner *et al.* 2012). A non-parallel wind or, in other words, the angle of attack β, $\beta < \pi$, of the large-scale circulation of a fluid inside a RBC cell against the heated/cooled horizontal plate, influences the flow characteristics within the boundary layers.

In the present work, in order to account for the influence of the angle $\beta \neq \pi$ and, hence, of the non-parallel and non-constant wind, we make use of the Falkner–Skan approximation of the boundary layers in turbulent thermal convection, which can be interpreted as an extension of the Prandtl–Blasius ansatz to a non-zero pressure change along the wind. As we show in the present work, this approach, compared to a Prandtl–Blasius one, leads to more reliable predictions of some integrated quantities related to the thicknesses of the thermal and viscous boundary layers.

Since our theoretical estimates are corroborated against the numerical data, we start the paper with a short description of the numerical ansatz (§ 2), then discuss the boundary layer equations (§ 3) and their own boundary conditions, i.e. the wind at the edge of the viscous boundary layer (§ 4). After that the solutions of the obtained system of the boundary layer equations as well as their limits for Prandtl numbers $\mathcal{P}r \ll 1$ and $\mathcal{P}r \gg 1$ are derived (§ 5). Finally, the balance between the thicknesses of the thermal and viscous boundary layers is discussed in § 6 and a corroboration of the theory with the numerical results, obtained in the DNS of turbulent RBC in water and air, are discussed in § 7.

2. Governing equations and DNS of turbulent RBC

We consider the following system of the governing momentum (2.1), (2.2), (2.3), energy (2.4) and continuity (2.5) equations for the Rayleigh–Bénard problem in Boussinesq approximation:

$$\widetilde{u}_{\widetilde{t}} + \widetilde{u}\widetilde{u}_{\widetilde{x}} + \widetilde{v}\widetilde{u}_{\widetilde{y}} + \widetilde{w}\widetilde{u}_{\widetilde{z}} + \widetilde{p}_{\widetilde{x}}/\widetilde{\rho} = \widetilde{\nu}\left(\widetilde{u}_{\widetilde{x}\widetilde{x}} + \widetilde{u}_{\widetilde{y}\widetilde{y}} + \widetilde{u}_{\widetilde{z}\widetilde{z}}\right), \tag{2.1}$$

$$\widetilde{v}_{\widetilde{t}} + \widetilde{u}\widetilde{v}_{\widetilde{x}} + \widetilde{v}\widetilde{v}_{\widetilde{y}} + \widetilde{w}\widetilde{v}_{\widetilde{z}} + \widetilde{p}_{\widetilde{y}}/\widetilde{\rho} = \widetilde{\nu}\left(\widetilde{v}_{\widetilde{x}\widetilde{x}} + \widetilde{v}_{\widetilde{y}\widetilde{y}} + \widetilde{v}_{\widetilde{z}\widetilde{z}}\right) + \widetilde{\alpha}\widetilde{g}(\widetilde{T} - \widetilde{T}_{\mathrm{mid}}), \tag{2.2}$$

$$\widetilde{w}_{\widetilde{t}} + \widetilde{u}\widetilde{w}_{\widetilde{x}} + \widetilde{v}\widetilde{w}_{\widetilde{y}} + \widetilde{w}\widetilde{w}_{\widetilde{z}} + \widetilde{p}_{\widetilde{z}}/\widetilde{\rho} = \widetilde{\nu}\left(\widetilde{w}_{\widetilde{x}\widetilde{x}} + \widetilde{w}_{\widetilde{y}\widetilde{y}} + \widetilde{w}_{\widetilde{z}\widetilde{z}}\right), \tag{2.3}$$

$$\widetilde{T}_{\widetilde{t}} + \widetilde{u}\widetilde{T}_{\widetilde{x}} + \widetilde{v}\widetilde{T}_{\widetilde{y}} + \widetilde{w}\widetilde{T}_{\widetilde{z}} = \widetilde{\kappa}\left(\widetilde{T}_{\widetilde{x}\widetilde{x}} + \widetilde{T}_{\widetilde{y}\widetilde{y}} + \widetilde{T}_{\widetilde{z}\widetilde{z}}\right), \tag{2.4}$$

$$\widetilde{u}_{\widetilde{x}} + \widetilde{v}_{\widetilde{y}} + \widetilde{w}_{\widetilde{z}} = 0, \tag{2.5}$$

where $\widetilde{u}$ and $\widetilde{w}$ are the horizontal components of the velocity along the axes $\widetilde{x}$ and $\widetilde{z}$, respectively, and $\widetilde{v}$ is the vertical component of the velocity along the axis $\widetilde{y}$, $\widetilde{t}$ denotes time and $\widetilde{p}$ the pressure. A variable marked as a subindex denotes the partial derivative with respect to this variable, e.g. $\widetilde{u}_{\widetilde{t}} \equiv \partial\widetilde{u}/\partial\widetilde{t}$, $\widetilde{u}_{\widetilde{x}} \equiv \partial\widetilde{u}/\partial\widetilde{x}$, etc. Further, $\widetilde{T}_{\mathrm{mid}}$ is the arithmetic mean of the top temperature $\widetilde{T}_{\mathrm{top}}$ and bottom temperature $\widetilde{T}_{\mathrm{bot}}$, $\widetilde{T}_{\mathrm{bot}} > \widetilde{T}_{\mathrm{top}}$, $\widetilde{\rho}$ denotes the density, $\widetilde{\nu}$ the kinematic viscosity, $\widetilde{\kappa}$ the thermal diffusivity, $\widetilde{\alpha}$ the isobaric thermal expansion coefficient and $\widetilde{g}$ the acceleration due to gravity. The velocity vanishes on the domain's boundary, according to the impermeability and no-slip boundary conditions, while the normal derivative of the temperature on the vertical wall is equal to zero, because of its adiabaticity.

Substituting the factorization $\widetilde{X} = \widetilde{X}_{ref}\, X$ for each dimensional variable $\widetilde{X}$ in the system (2.1)–(2.5), where X is a dimensionless variable and $\widetilde{X}_{ref}$ the corresponding

$\mathcal{P}r$	$\mathcal{R}a$	N_r	N_ϕ	N_z	n_T	$\check{n}_T$	n_u	$\check{n}_u$	$\mathcal{N}u$	τ
0.786	10^7	96	256	192	8	4	8	3	16.9±0.2	3775
	10^8	192	512	384	11	5	11	5	31.9±0.2	1240
	10^9	384	1024	768	13	7	12	6	63.1±0.4	318
4.380	10^7	64	512	128	6	3	9	5	16.2±0.5	200
	10^8	192	512	384	9	4	14	6	32.9±0.2	760
	10^9	384	512	768	16	6	25	9	64.7±0.7	250

TABLE 1. DNS parameters for the Prandtl number 0.786 and 4.38: the number of mesh nodes in the direction N_i $(i = r; \phi; z)$, the number of nodes in the thermal and viscous BLs as used in the DNS (n_T and n_u) and as required by theory (Shishkina *et al.* 2010) ($\check{n}_T$ and $\check{n}_u$), the Nusselt number $\mathcal{N}u$ with its maximal deviation and the number of dimensionless time units τ used for the statistical averaging. The data for $\mathcal{P}r = 0.786$ are adopted from Wagner *et al.* (2012).

reference value, $\widetilde{x}_{ref} = \widetilde{D}$, $\widetilde{u}_{ref} = \left(\widetilde{\alpha}g\widetilde{D}\,\widetilde{\Delta}\right)^{1/2}$, $\widetilde{t}_{ref} = \widetilde{x}_{ref}/\widetilde{u}_{ref}$, $\widetilde{T} - \widetilde{T}_{\mathrm{mid}} = \widetilde{\Delta}T$, $\widetilde{\Delta} \equiv \widetilde{T}_{\mathrm{bot}} - \widetilde{T}_{\mathrm{top}}$, $\widetilde{p}_{ref} = \widetilde{u}^2_{ref}\,\widetilde{\rho}$, $\widetilde{D}$ the width of the container and $\widetilde{H}$ its height, we obtain the following system of dimensionless equations:

$$
\begin{aligned}
u_t + uu_x + vu_y + wu_z + p_x &= \Gamma^{-3/2}\mathcal{R}a^{-1/2}\mathcal{P}r^{1/2}(u_{xx} + u_{yy} + u_{zz}),\\
v_t + uv_x + vv_y + wv_z + p_y &= \Gamma^{-3/2}\mathcal{R}a^{-1/2}\mathcal{P}r^{1/2}(v_{xx} + v_{yy} + v_{zz}) + T,\\
w_t + uw_x + vw_y + ww_z + p_z &= \Gamma^{-3/2}\mathcal{R}a^{-1/2}\mathcal{P}r^{1/2}(w_{xx} + w_{yy} + w_{zz}),\\
T_t + uT_x + vT_y + wT_z &= \Gamma^{-3/2}\mathcal{R}a^{-1/2}\mathcal{P}r^{-1/2}(T_{xx} + T_{yy} + T_{zz}),\\
u_x + v_y + w_z &= 0,
\end{aligned}
\tag{2.6}
$$

Here $\mathcal{R}a$ and $\mathcal{P}r$ are the Rayleigh number and Prandtl number,

$$\mathcal{R}a = \widetilde{\alpha}\widetilde{g}\widetilde{\Delta}\widetilde{H}^3/(\widetilde{\nu}\widetilde{\kappa}), \qquad \mathcal{P}r = \widetilde{\nu}/\widetilde{\kappa},$$

respectively, and $\Gamma \equiv \widetilde{D}/\widetilde{H}$ is the aspect ratio. The dimensionless temperature varies between $T_{\mathrm{bot}} = 0.5$ at the bottom and $T_{\mathrm{top}} = -0.5$ at the top horizontal walls and satisfies $\partial T/\partial \mathbf{n} = 0$ on the vertical walls, where $\mathbf{n}$ is the normal vector. All velocity components are equal to zero on the domain's boundary.

DNS of turbulent RBC in air and water in a cylindrical domain of the aspect ratio $\Gamma = 1$ are performed using the same finite-volume code as in Shishkina & Wagner (2005), Horn *et al.* (2011). The computational grids used in the DNS resolve Kolmogorov and Batchelor scales in the whole domain. According the conducted *a posteriori* grid resolution analysis, we take up to two times more grid nodes within the thermal and viscous boundary layers than in the theoretical estimates derived in Shishkina *et al.* (2010) for the minimally required numbers of the nodes, N_{th} and N_v, respectively. Further details on the conducted DNS can be found in table 1.

In figure 1 one can see temperature patterns, or so-called sheet-like plumes, which develop at the edges of the thermal boundary layers. These snapshots are obtained in the DNS of turbulent RBC for $\mathcal{R}a = 10^7$, 10^8 and 10^9 and $\mathcal{P}r = 0.786$ (air) and $\mathcal{P}r = 4.38$ (water). The direction of the wind can already be visually identified in the instantaneous temperature fields, presented in figure 1. The horizontal cross-sections are arranged in such a way that the mean LSC above the viscous boundary layer goes from left to right. Thus, the cold fluid from the top hits the lower hot boundary layer at the left side, the wind blows along the plate and sweeps up material along its path, resulting in smaller structures on the right side, which then detach as plumes and move upwards.

More qualitatively, the directions of the mean wind are evaluated in the same way as it was done in Wagner *et al.* (2012). For each simulation we first determine the time periods without serious changes of the local wind direction, i.e. without cessations and reversals of the large-scale circulation (Funfschilling & Ahlers 2004; Xi & Xia 2007; Kaczorowski *et al.* 2011; Weiss & Ahlers 2011; Xia 2011). The wind direction is extracted in a similar way as in Brown & Ahlers (2006), based on the information on the temperature distribution at the vertical wall at the height $H/2$ from the bottom. Once the time period and the direction of the mean LSC are fixed, we conduct the time averaging of the main flow characteristics in the vertical cross-section, which corresponds to the LSC, and in another vertical cross-section, which is orthogonal to it ($\mathrm{LSC}_\perp$).

In figure 2 one can see distributions of the time-averaged temperature in the LSC- and $\mathrm{LSC}_\perp$-planes for $\mathcal{R}a = 10^8$ and both considered operating fluids. The arrows there show the directions of the mean velocity vectors. As one can see for both fluids, in the LSC-plane there are three relatively large rolls: the LSC itself, which has a counterclockwise direction of rotation, and two secondary rolls, which locate in the upper right and lower left corners and rotate in the clockwise direction. In the plane, orthogonal to LSC ($\mathrm{LSC}_\perp$) one observes four-roll structures, also for both fluids. Here at a half height from the bottom the fluid moves from the vertical walls towards the center.

Note that the mean flow distributions presented in figure 2, although looking two-dimensional (2D), are obtained in well-resolved three-dimensional (3D) DNS of turbulent RBC in a cylinder. In the next paragraphs we develop and check our theoretical estimates against the numerical data obtained in these DNS.

3. Boundary layer equations

In this section we develop the boundary layer equations, which solutions approximate the temperature and velocity fields within the laminar viscous boundary layers in Rayleigh–Bénard convection. Here we admit a non-zero pressure gradient along the considered horizontal isothermal wall.

Without restriction of generality we assume that the coordinate system $(\widetilde{x}, \widetilde{y}, \widetilde{z})$ is chosen in such a way that at the edge of the viscous boundary layer the horizontal $\widetilde{z}$-component of the wind is negligible, compared to its other horizontal component along the $\widetilde{x}$-axis. Thus, taking $\widetilde{w} \equiv 0$ in the equations (2.1)–(2.5) and assuming that the flow is laminar within the viscous boundary layer and, hence, the time dependences of the flow components are negligible, one obtains the following system of equation for the steady and two-dimensional boundary-layer flow:

$$\widetilde{u}\widetilde{u}_{\widetilde{x}} + \widetilde{v}\widetilde{u}_{\widetilde{y}} + \widetilde{p}_{\widetilde{x}}/\widetilde{\rho} = \widetilde{\nu}\widetilde{u}_{\widetilde{x}\widetilde{x}} + \widetilde{\nu}\widetilde{u}_{\widetilde{y}\widetilde{y}}, \tag{3.1}$$

$$\widetilde{u}\widetilde{v}_{\widetilde{x}} + \widetilde{v}\widetilde{v}_{\widetilde{y}} + \widetilde{p}_{\widetilde{y}}/\widetilde{\rho} = \widetilde{\nu}\widetilde{v}_{\widetilde{x}\widetilde{x}} + \widetilde{\nu}\widetilde{v}_{\widetilde{y}\widetilde{y}} + \widetilde{\alpha}\widetilde{g}(\widetilde{T} - \widetilde{T}_{\mathrm{mid}}), \tag{3.2}$$

$$\widetilde{u}\widetilde{T}_{\widetilde{x}} + \widetilde{v}\widetilde{T}_{\widetilde{y}} = \widetilde{\kappa}\widetilde{T}_{\widetilde{x}\widetilde{x}} + \widetilde{\kappa}\widetilde{T}_{\widetilde{y}\widetilde{y}}, \tag{3.3}$$

$$\widetilde{u}_{\widetilde{x}} + \widetilde{v}_{\widetilde{y}} = 0. \tag{3.4}$$

Following Prantl's ansatz (Schlichting & Gersten 2000), we estimate separately the order of magnitude of each component in the above equations. The viscous boundary layer is thin and, hence, $\widetilde{\delta}_u(\widetilde{x}) \ll \widetilde{x}$, where $\widetilde{\delta}_u$ is the thickness of the viscous boundary layer. For the representative length $\widetilde{L}$ in the horizontal direction holds $\widetilde{x} \sim \widetilde{L}$, $\widetilde{y} \sim \widetilde{\delta}_u$. Assuming that $\partial a/\partial b \sim a/b$ for any a and b and that $\widetilde{u} \sim \widetilde{U}$, where $\widetilde{U}$ is the horizontal component of the wind velocity above the boundary layer, from the continuity equation (3.4) one obtains that $\widetilde{v} \sim \widetilde{U}\widetilde{\delta}_u/\widetilde{L}$.

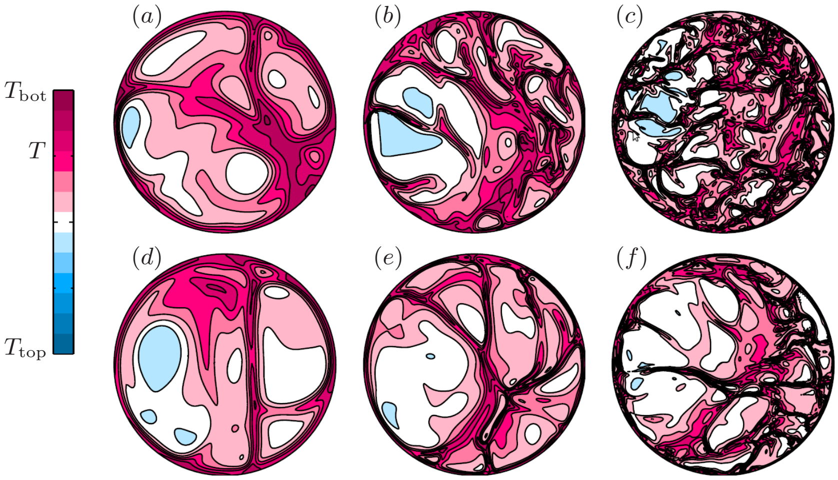

FIGURE 1. Instantaneous temperature distribution at the edges of the thermal boundary layers, as obtained in DNS of turbulent RBC for $\mathcal{R}a = 10^7$ (a, d), 10^8 (b, e) and 10^9 (c, f) for air (a, b, c), $\mathcal{P}r = 0.786$, and water (d, e, f), $\mathcal{P}r = 4.38$. Here the mean wind above the viscous boundary layer goes from left to right.

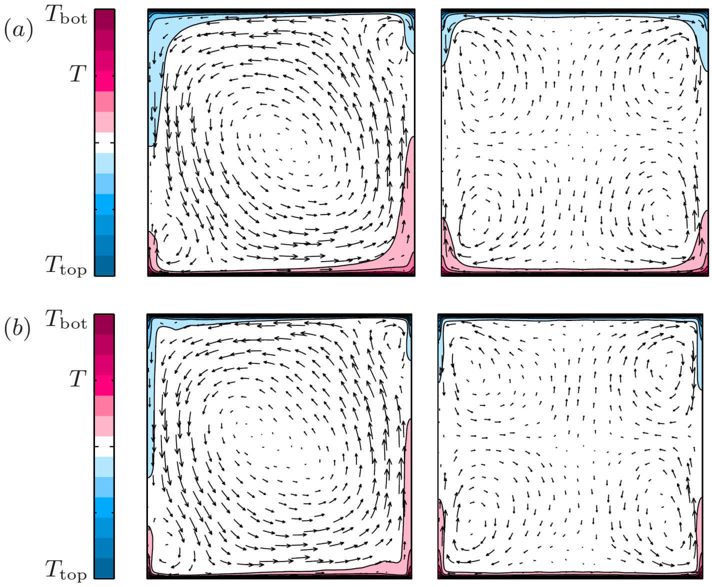

FIGURE 2. Distributions of the time-averaged temperature in the vertical planes of LSC (left) and LSC$_\perp$ (right), as obtained in DNS of turbulent RBC for $\mathcal{R}a = 10^8$ for (a) air, $\mathcal{P}r = 0.786$, and (b) water, $\mathcal{P}r = 4.38$. The arrows show the mean velocity (wind) vectors.

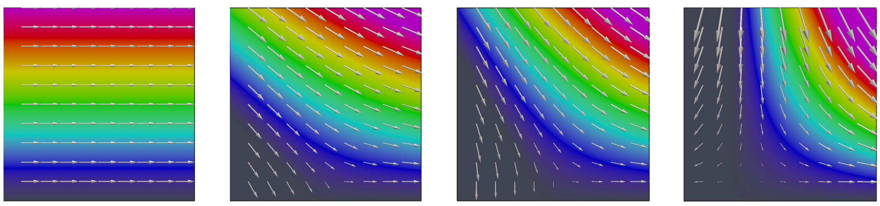

$m = 0,\ \beta = \pi$ $\quad m = 1/3,\ \beta = 3\pi/4$ $\quad m = 1/2,\ \beta = 2\pi/3$ $\quad m = 1,\ \beta = \pi/2$

FIGURE 3. Streamfunctions (colours) for flows inside corners of the size $\beta = \pi/(m+1)$ for $m = 0$ (Prandtl–Blasius flow), $m = 1/3$, $m = 1/2$ and $m = 1$ (stagnation-point flow). The arrows show the velocity vectors with the components $\widetilde{U}_r$ (4.13) and $\widetilde{U}_\phi$ (4.14).

Further, the orders of magnitude of the first components $\widetilde{*}_{\widetilde{x}\widetilde{x}}$ in the right-hand sides of (3.1)–(3.3) are much smaller that those of the second ones $\widetilde{*}_{\widetilde{y}\widetilde{y}}$, and therefore they are negligible. Assuming that the rest components in the momentum equation (3.1) are of the same order, one obtains that the order of magnitude of the pressure is $\widetilde{p} \sim \widetilde{\rho}\widetilde{U}^2$ and that $\widetilde{\delta}_u/\widetilde{L} \sim Re^{-1/2}$, $Re \equiv \widetilde{L}\widetilde{U}/\widetilde{\nu}$, $Re \gg 1$.

In the equation (3.2), the orders of magnitude of the components $\widetilde{u}\widetilde{v}_{\widetilde{x}} \sim \widetilde{v}\widetilde{v}_{\widetilde{y}} \sim \widetilde{\delta}_u\widetilde{U}^2/\widetilde{L}^2$ and $\widetilde{\nu}\widetilde{v}_{\widetilde{y}\widetilde{y}} \sim \widetilde{\nu}\widetilde{U}/(\widetilde{L}\widetilde{\delta}_u)$ are much smaller than the order of magnitude of the component $\widetilde{p}_{\widetilde{y}}/\widetilde{\rho} \sim \widetilde{U}^2/\widetilde{\delta}_u$ if $Re \gg 1$. For the buoyancy term one obtains: $\widetilde{\alpha}\widetilde{g}(\widetilde{T} - \widetilde{T}_{\mathrm{mid}}) \sim \widetilde{\alpha}\widetilde{g}\widetilde{\Delta}$. As it was shown in Wagner *et al.* (2012), in turbulent Rayleigh–Bénard convection the wind velocity $\widetilde{U}$ is of the same order of magnitude as the free-fall velocity $\sqrt{\widetilde{\alpha}\widetilde{g}\widetilde{\Delta}\widetilde{L}}$, therefore in the equation (3.2) the buoyancy term, being of order $\sim \widetilde{\alpha}\widetilde{g}\widetilde{\Delta}$, is also negligible compared to the pressure term $\widetilde{p}_{\widetilde{y}}/\widetilde{\rho} \sim \widetilde{\alpha}\widetilde{g}\widetilde{\Delta}(\widetilde{L}/\widetilde{\delta}_u)$. (Note, that this boundary layer model differs from the Stewartson (1958) model for a very slow wind $\widetilde{U} \ll \sqrt{\widetilde{\alpha}\widetilde{g}\widetilde{\Delta}\widetilde{L}}$ above the viscous boundary layer, where the buoyancy cannot be neglected.)

Thus instead of the equations (3.1)–(3.3), one can consider the following system of equations within the boundary layer:

$$\widetilde{u}\widetilde{u}_{\widetilde{x}} + \widetilde{v}\widetilde{u}_{\widetilde{y}} = \widetilde{\nu}\widetilde{u}_{\widetilde{y}\widetilde{y}} - \widetilde{p}_{\widetilde{x}}/\widetilde{\rho}, \tag{3.5}$$

$$0 = -\widetilde{p}_{\widetilde{y}}/\widetilde{\rho}, \tag{3.6}$$

$$\widetilde{u}\widetilde{T}_{\widetilde{x}} + \widetilde{v}\widetilde{T}_{\widetilde{y}} = \widetilde{\kappa}\widetilde{T}_{\widetilde{y}\widetilde{y}}, \tag{3.7}$$

respectively. Relations (3.5),(3.6) and (3.7) are known as Prandtl (1905) and Pohlhausen (1921) equations, respectively. With respect to Rayleigh–Bénard convection, equation (3.5) is often considered with neglected pressure term $\widetilde{p}_{\widetilde{x}}/\widetilde{\rho}$, as in the case of a parallel flow over a flat plate (Blasius 1908). Following tradition, throughout the paper we call the reference case (3.5),(3.6) and (3.7) with zero pressure term $\widetilde{p}_{\widetilde{x}}/\widetilde{\rho}$ the Prandtl–Blasius one.

Since the considered flow is two-dimensional and incompressible, let us further introduce the streamfunction $\widetilde{\Psi}$, which satisfies $\widetilde{u} = \widetilde{\Psi}_{\widetilde{y}}$ and $\widetilde{v} = -\widetilde{\Psi}_{\widetilde{x}}$. One can rewrite the equations (3.5), (3.7) in terms of the streamfunction $\widetilde{\Psi}$ as follows:

$$\widetilde{\Psi}_{\widetilde{y}}\widetilde{\Psi}_{\widetilde{y}\widetilde{x}} - \widetilde{\Psi}_{\widetilde{x}}\widetilde{\Psi}_{\widetilde{y}\widetilde{y}} = \widetilde{\nu}\widetilde{\Psi}_{\widetilde{y}\widetilde{y}\widetilde{y}} - \widetilde{p}_{\widetilde{x}}/\widetilde{\rho}, \tag{3.8}$$

$$\widetilde{\Psi}_{\widetilde{y}}\widetilde{T}_{\widetilde{x}} - \widetilde{\Psi}_{\widetilde{x}}\widetilde{T}_{\widetilde{y}} = \widetilde{\kappa}\widetilde{T}_{\widetilde{y}\widetilde{y}}. \tag{3.9}$$

Similarity solutions of these equations are sought with respect to a certain similarity variable ξ, assuming that $\widetilde{\Psi}$ and ξ are representable in the following forms:

$$\widetilde{\Psi} = \widetilde{\nu}\Psi(\xi)\, g(x), \tag{3.10}$$

$$\xi = y\, f(x), \tag{3.11}$$

where

$$x \equiv \widetilde{x}/\widetilde{L}, \qquad y \equiv \widetilde{y}/\widetilde{L} \tag{3.12}$$

and the horizontal component of the velocity (wind) at the edge of the viscous boundary layer is independent from the vertical coordinate $\widetilde{y}$, i.e. $\widetilde{U} = \widetilde{U}(\widetilde{x})$. Here Ψ, g and f are dimensionless functions and $\widetilde{L}$ is a representative length in the horizontal direction.

3.1. *Energy equation*

Using relations (3.10), (3.11) and representing the temperature as

$$\widetilde{T} = \widetilde{T}_{\mathrm{bot}} - \Theta\widetilde{\Delta}/2, \tag{3.13}$$

where $\Theta = \Theta(\xi)$ is dimensionless temperature, from (3.9) one obtains the following energy equation

$$\widetilde{\kappa} f^2 \Theta_{\xi\xi} + \widetilde{\nu} f g_x \Psi \Theta_\xi = 0.$$

Here and in the following, g_x and f_x denote the derivatives with respect to x (3.12) of the functions g and f, respectively. Since a non-trivial solution is sought, $f \neq 0$, for the existence of a similarity solution the requirement

$$g_x/f = a, \qquad a = const., \tag{3.14}$$

must be fulfilled. Putting $a = 1$ one finishes with the following energy boundary layer equation:

$$\Theta_{\xi\xi} + \mathcal{P}r\,\Psi\Theta_\xi = 0. \tag{3.15}$$

3.2. *Momentum equation*

Under assumptions (3.10), (3.11) the momentum equation (3.8) reads as

$$\frac{\widetilde{\nu}^2}{\widetilde{L}^3}\left(fg(fg)_x(\Psi_\xi)^2 - f^2 g g_x \Psi\Psi_{\xi\xi}\right) = \frac{\widetilde{\nu}^2}{\widetilde{L}^3} f^3 g \Psi_{\xi\xi\xi} - \frac{\widetilde{p}_{\widetilde{x}}}{\widetilde{\rho}}.$$

Again, since a non-trivial solution is sought, $f \neq 0$, $g \neq 0$, one obtains

$$\frac{(fg)_x}{f^2}(\Psi_\xi)^2 - \frac{g_x}{f}\Psi\Psi_{\xi\xi} = \Psi_{\xi\xi\xi} - \frac{\widetilde{p}_{\widetilde{x}}}{\widetilde{\rho} f^3 g}\frac{\widetilde{L}^3}{\widetilde{\nu}^2}. \tag{3.16}$$

At the edge of the viscous boundary layer the viscous effects become less important, which together with the independence of the horizontal component of the wind from the vertical coordinate leads to the following approximation of the pressure term there:

$$\widetilde{U}\widetilde{U}_{\widetilde{x}} = -\frac{\widetilde{p}_{\widetilde{x}}}{\widetilde{\rho}} \qquad \Longrightarrow \qquad -\frac{\widetilde{p}_{\widetilde{x}}}{\widetilde{\rho} f^3 g}\frac{\widetilde{L}^3}{\widetilde{\nu}^2} = \frac{(\widetilde{U}^2)_{\widetilde{x}}}{2f^3 g}\frac{\widetilde{L}^3}{\widetilde{\nu}^2}.$$

Since the pressure gradient remains unchanged in the vertical y-direction within the boundary layer, cf. (3.6), from this and (3.16) one obtains

$$\frac{(fg)_x}{f^2}(\Psi_\xi)^2 - \frac{g_x}{f}\Psi\Psi_{\xi\xi} = \Psi_{\xi\xi\xi} + \frac{(\widetilde{U}^2)_{\widetilde{x}}}{2f^3 g}\frac{\widetilde{L}^3}{\widetilde{\nu}^2}. \tag{3.17}$$

For the existence of a similarity solution, all the coefficients in this equation must be constant and the free term might be a function of ξ or a constant. This together with (3.14) leads to the requirement

$$\frac{g g_{xx}}{(g_x)^2} = c, \qquad c = const.$$

Dependently on the constant c, the function g can take forms

$$g(x) = \begin{cases} B\exp(bx), & c = 1, \\ B(x+d)^n, & c \neq 1,\ n = (1-c)^{-1}, \end{cases} \tag{3.18}$$

with certain constants B, b and d. Without loss of generality one may further assume that $d=0$. Equation (3.17) can then be rewritten as

$$(c+1)(\Psi_\xi)^2 - \Psi\Psi_{\xi\xi} = \Psi_{\xi\xi\xi} + \frac{(\widetilde{U}^2)_{\widetilde{x}}}{2(g_x)^3 g}\frac{\widetilde{L}^3}{\widetilde{\nu}^2}. \tag{3.19}$$

4. Wind at the edge of the viscous boundary layer

According to the two possible representations of function g (3.18), in this section we consider two different types of wind, which admit similarity solutions of the boundary layer equations.

4.1. *Wind as an exponential function*

Let us consider the first case, i.e. $c=1$ and $g(x)=B\exp(bx)$. Together with the equations (3.10), (3.11) and relation (3.14) the streamfunction

$$\widetilde{\Psi} = \widetilde{\nu}\Psi(\xi)B\exp(bx) \tag{4.1}$$

and the similarity variable

$$\xi = ybB\exp(bx) \tag{4.2}$$

are obtained. Placed into the differential equation (3.19) it turns out that a similarity solution can be obtained if the wind $\widetilde{U}$ has the form

$$\widetilde{U} = \widetilde{U}_0\exp(kx) \tag{4.3}$$

and the relations

$$B = \sqrt{\frac{2}{k}}\sqrt{\frac{\widetilde{L}\widetilde{U}_0}{\widetilde{\nu}}}, \qquad b = \frac{k}{2}$$

hold. The momentum boundary layer equation (3.19) takes then the following form:

$$\Psi_{\xi\xi\xi} + \Psi\Psi_{\xi\xi} + 2 - 2(\Psi_\xi)^2 = 0. \tag{4.4}$$

Taking $\xi=1$ and $y=\widetilde{\delta}_u/\widetilde{L}$, where $\widetilde{\delta}_u$ is the viscous boundary layer thickness, from (4.2) one obtains that $\widetilde{\delta}_u$ develops in the horizontal direction $\widetilde{x}$ as

$$\widetilde{\delta}_u \sim \sqrt{\frac{\widetilde{\nu}\widetilde{L}}{\widetilde{U}_0}}\exp(-kx/2). \tag{4.5}$$

Therefore, for the local Reynolds number $Re=\widetilde{L}\widetilde{U}/\widetilde{\nu}$, based on the wind $\widetilde{U}$ (4.3), one obtains

$$\delta_u \equiv \widetilde{\delta}_u/\widetilde{L} \sim Re^{-1/2}. \tag{4.6}$$

Note that, according to the above model and relations (4.3), (4.5), the boundary layer thickness should decrease (increase) along x if the wind magnitude increases (decreases) with growing x. In contrast to this, our DNS of turbulent Rayleigh–Bénard convection (Wagner *et al.* 2012) showed that near the horizontal plate, after the stagnation point, the boundary layer thickness grows together with the wind magnitude (see also Calzavarini *et al.* (2006)). Therefore the next possible similarity solution for a wind, which can be represented as a power function, seems to be more relevant with respect to Rayleigh–Bénard convection.

4.2. *Wind as a power function*

In the second case, for $g = Bx^n$, the streamfunction $\widetilde{\Psi}$ and the similarity variable ξ equal, respectively,

$$\widetilde{\Psi} = \widetilde{\nu}\Psi B x^n, \tag{4.7}$$

$$\xi = yBnx^{n-1}. \tag{4.8}$$

If the wind $\widetilde{U}$ has the form

$$\widetilde{U} = \widetilde{U}_0 x^m, \tag{4.9}$$

and the relations

$$B = \sqrt{\frac{2}{m+1}}\sqrt{\frac{\widetilde{L}\widetilde{U}_0}{\widetilde{\nu}}}, \qquad n = \frac{m+1}{2}$$

hold, from this and (3.19) one obtains the Falkner & Skan (1931) equation

$$\Psi_{\xi\xi\xi} + \Psi\Psi_{\xi\xi} + \frac{2m}{m+1}(1 - (\Psi_\xi)^2) = 0. \tag{4.10}$$

Further, (4.8) reveals for $\xi = C = const.$ and $y = \widetilde{\delta}_u$ that

$$\widetilde{\delta}_u = C\sqrt{\frac{2}{m+1}x^{1-m}}\sqrt{\frac{\widetilde{\nu}\widetilde{L}}{\widetilde{U}_0}}. \tag{4.11}$$

Hence, for the dimensionless boundary layer thickness δ_u and Reynolds number based on the wind $\widetilde{U}$ (4.9), the following relation holds:

$$\delta_u \equiv \frac{\widetilde{\delta}_u}{\widetilde{L}} \sim \sqrt{\frac{x}{Re}}. \tag{4.12}$$

Note, the relation (4.12) holds for the Prandtl–Blasius boundary layer ($m = 0$) as well as for general Falkner–Skan boundary layers and is one of the main assumptions in the Grossmann & Lohse (2000) theory on scaling in thermal convection for the case of non-turbulent boundary layers (see also Grossmann & Lohse (2001, 2011); Stevens *et al.* (2013)).

4.3. *Appearance of the power-function wind in the core flow*

Following Falkner & Skan (1931), one can show that the wind $\widetilde{U}$ (4.9) might appear in a corner flow along the corners' sides. Indeed, let us consider a core flow, which velocity components in polar coordinates (r, ϕ) are determined as

$$\widetilde{U}_r = \widetilde{U}_0 r^m \cos((m+1)\phi), \tag{4.13}$$

$$\widetilde{U}_\phi = -\widetilde{U}_0 r^m \sin((m+1)\phi). \tag{4.14}$$

The velocity component $\widetilde{U}_\phi$ of such flow vanishes if $\phi = j\pi/(m+1)$, $j = 0, 1, 2, ...$ A sketch of this flow and the corresponding polar coordinate system are presented in figure 4 and the streamfunctions of the flow (4.13), (4.14) for different m are presented in figure 3.

One can see that this flow can be interpreted as a flow along the sides of a corner, which size is equal to

$$\beta = \pi/(m+1). \tag{4.15}$$

On the surfaces of the corner, e.g. when $\phi = 0$, the velocity varies as a power function

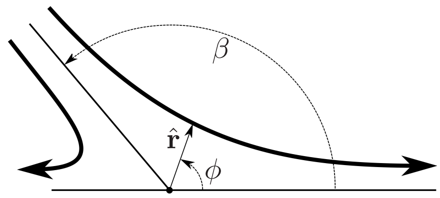

FIGURE 4. Sketch of the power-function wind and the corresponding polar coordinate system (r, ϕ), with $\hat{\boldsymbol{r}}$ being the radial unit vector and β the corner angle as defined in (4.15).

on the distance r along the surface. Thus, in Cartesian coordinate system for $\phi = 0$ the horizontal velocity can be presented as a power function on the coordinate x.

Comparing the LSC of the fluid in the core region, obtained in the DNS of turbulent RBC (figure 2, left) with the streamlines in figure 3, one concludes that the wind in turbulent RBC, which slides off from the secondary rolls and then flows along the lower horizontal wall with a pitch angle β, $\beta \in [\frac{\pi}{2}, \frac{3\pi}{4}]$, is similar to a flow inside a corner of the size β. This together with the relation (4.15) make it clear that the wind can be approximated by a power function of the form (4.13), (4.14) with $m \in [1/3; 1]$.

5. Solutions of the boundary layer equations and their limits

5.1. *Horizontal velocity and temperature profiles*

Vertical profiles of the temperature and horizontal velocity near the horizontal plates are main flow characteristics and their investigation is a part of any RBC study (Tilgner *et al.* 1993; Ching 1997; du Puits *et al.* 2007; Gauthier & Roche 2008; Sun *et al.* 2008; Shishkina & Thess 2009; Stevens *et al.* 2010; Zhou & Xia 2010; Scheel *et al.* 2012; Verzicco 2012; Stevens *et al.* 2012; Ahlers *et al.* 2012; Grossmann & Lohse 2012). Usually they are compared against the predictions for laminar boundary layers, based on the Prandtl–Blasius ansatz, which is a particular case of the more general Falkner–Skan approach.

Therefore in this section we study the temperature and velocity profiles, which one can obtain within the general Falkner–Skan approximation. Further we derive the limits of the temperature profiles for the general Falkner–Skan approximation and prove that these limits are the same for the Prandtl–Blasius approximation and for the general Falkner–Skan approximation.

Based on the results of the previous section, let us consider the following system of the momentum (Falkner–Skan)

$$\begin{gathered}\Psi_{\xi\xi\xi} + \Psi\Psi_{\xi\xi} + \frac{2m}{m+1}\left(1-(\Psi_\xi)^2\right) = 0, \\ \Psi(0)=0, \quad \Psi_\xi(0)=0, \quad \Psi_\xi(\infty)=1,\end{gathered} \tag{5.1}$$

and energy

$$\begin{gathered}\Theta_{\xi\xi} + \mathcal{P}r\,\Psi\Theta_\xi = 0, \\ \Theta(0)=0, \qquad \Theta(\infty)=1.\end{gathered} \tag{5.2}$$

boundary layer equations with respect to Rayleigh–Bénard convection.

One can solve these equations numerically (Falkner & Skan 1931; Wilcox 2010). The solution of the momentum equation (5.1) depends only on m, while that of the energy one (5.2) depends also on Prandtl number. In figure 5 (a) the profiles of Ψ_ξ (horizontal velocity component) are presented for different values of m that is associated with a core

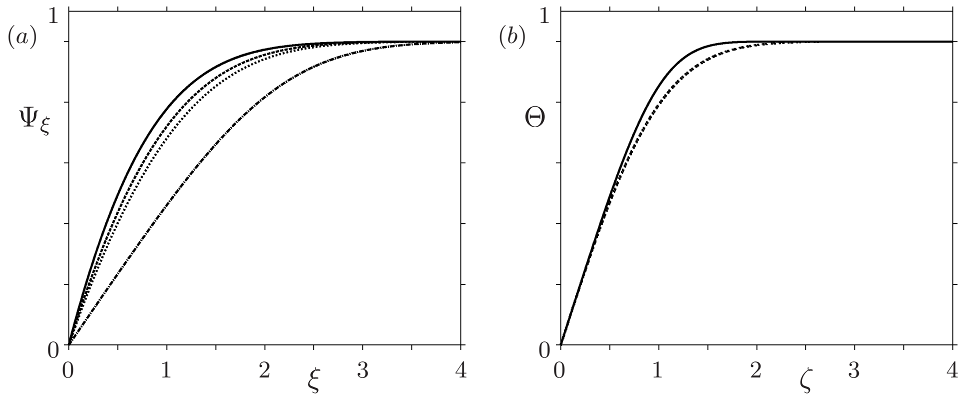

FIGURE 5. (a) Solutions of the Falkner–Skan equation for $m = 0$ (Prandtl–Blasius flow, -·-), $m = 1/3$ (···), $m = 1/2$ (- -) and $m = 1$ (stagnation-point flow, —). (b) Limiting cases $\Theta(\zeta) = \int_0^\zeta \exp(-B\chi^\omega)\,\mathrm{d}\chi$ for the rescaled temperature profiles for all values of m: $\mathcal{P}r \ll 1$ ($\omega = 2,\ B = \pi/4$, - -) and $\mathcal{P}r \gg 1$ ($\omega = 3,\ B = \Gamma^3(4/3) \approx 0.712$, —).

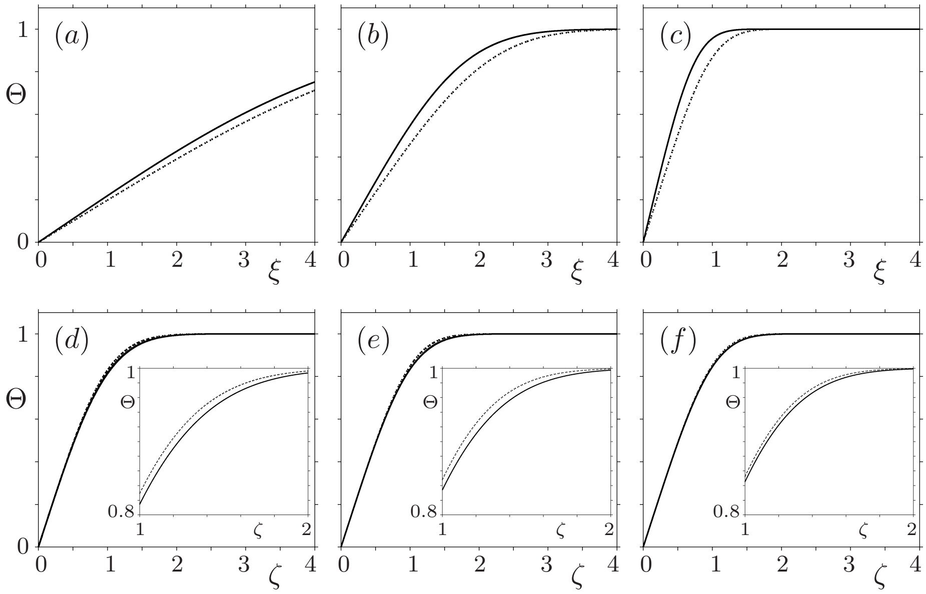

FIGURE 6. Temperature profiles with respect to the similarity variable ξ (a, b, c) and rescaled temperature profiles with respect to the similarity variable $\zeta = \xi\,\Theta_\xi(0)$ (d, e, f) for $\mathcal{P}r = 0.1$ (a, d), $\mathcal{P}r = 1$ (b, e), $\mathcal{P}r = 10$ (c, f) and $m = 0$ (Prandtl–Blasius flow, - -), $m = 1$ (stagnation-point flow, —).

flow in a corner $\beta = \pi/(m+1)$. Therefore the presented cases $m = 0$, $m = 1/3$, $m = 1/2$ and $m = 1$ correspond, respectively, to a Prandtl–Blasius flow over a horizontal plate, flows in corners $3\pi/4$ and $2\pi/3$ and a stagnation-point flow in a right-angle corner. In figure 6 (a, b, c) the temperature profiles are presented for particular cases $m = 0$ and $m = 1$, for Prandtl numbers 0.1, 1 and 10.

Although the solution of the energy boundary layer equation (5.2) depends strongly on m and $\mathcal{P}r$, the rescaled temperature profiles with respect to a similarity variable $\zeta = \xi\Theta_\xi(0)$ demonstrates only a week dependence on m (see figure 6 (d, e, f)). The choice of the similarity variable ζ provides the temperature derivative (with respect to ζ) equal to 1 at the plate, $\Theta_\zeta(0) = 1$. In order to understand the reasons for such a conjunction of the rescaled profiles for a Prandtl–Blasius approximation ($m = 0$) and stagnation-point approximation ($m = 1$) for a fixed Prandtl number, we further derive the limiting cases of the rescaled temperature profiles for $\mathcal{P}r \ll 1$ and $\mathcal{P}r \gg 1$.

5.2. *Limiting cases of the temperature profiles for all m*

5.2.1. *Case $\mathcal{P}r \ll 1$*

If the Prandtl number is much smaller than one, the thickness of the viscous boundary layer $\widetilde{\delta}_u$ is smaller than that of the thermal boundary layer $\widetilde{\delta}_\theta$. Therefore for infinitely small Prandtl numbers in the most part of the thermal boundary layer the horizontal component of the velocity is equal to the wind (4.9). Due to the continuity equation the corresponding vertical component of the velocity is equal to

$$\widetilde{V} = -m\,\widetilde{U}_0 \frac{\widetilde{x}^{m-1}\widetilde{y}}{\widetilde{L}^m}$$

and the thermal boundary layer equation (3.7) is reduced to

$$\widetilde{U}\widetilde{T}_{\widetilde{x}} + \widetilde{V}\widetilde{T}_{\widetilde{y}} = \widetilde{\kappa}\widetilde{T}_{\widetilde{y}\widetilde{y}}.$$

With the similarity variable

$$\zeta = \widetilde{y}\sqrt{\frac{(1+m)\widetilde{U}(x)}{\pi\widetilde{\kappa}\widetilde{x}}} = \sqrt{\frac{\widetilde{U}_0(1+m)}{\pi\widetilde{\kappa}\widetilde{L}^m}}\widetilde{y}\widetilde{x}^{(m-1)/2} \tag{5.3}$$

for the function Θ, defined by (3.13), one obtains the following equation:

$$\Theta_{\zeta\zeta} + \frac{\pi}{2}\zeta\Theta_\zeta = 0 \tag{5.4}$$

with the solution

$$\Theta(\zeta) = \int_0^\zeta \exp(-\frac{\pi}{4}\chi^2)d\chi. \tag{5.5}$$

This function is presented in figure 5 (*b*) with a dashed line. The choice of the similarity variable ζ (5.3) provides the solution (5.5) with the boundary conditions

$$\Theta(0) = 0, \quad \Theta_\zeta(0) = 1, \quad \Theta(\infty) = 1. \tag{5.6}$$

From the definition of the similarity variable ζ (5.3) one further obtains the scaling of the thermal boundary layer thickness:

$$\widetilde{\delta}_\theta \sim \sqrt{\frac{\widetilde{\kappa}\widetilde{x}}{\widetilde{U}(x)}} = \sqrt{\frac{\widetilde{x}/\widetilde{L}}{Re\mathcal{P}r}}\widetilde{L} \qquad \Longrightarrow$$

$$\delta_\theta \equiv \frac{\widetilde{\delta}_\theta}{\widetilde{L}} \sim Re^{-1/2}\mathcal{P}r^{-1/2}\left(\frac{\widetilde{x}}{\widetilde{L}}\right)^{1/2} \tag{5.7}$$

with local Reynolds number $Re = \widetilde{L}\widetilde{U}/\widetilde{\nu}$.

5.2.2. *Case $\mathcal{P}r \gg 1$*

For the Prandtl number much larger than one, the thickness of the thermal boundary layer $\widetilde{\delta}_\theta$ is smaller than that of the viscous boundary layer $\widetilde{\delta}_u$. For very large Prandtl numbers, in the thermal boundary layer the horizontal component of the velocity is a linear function of the vertical coordinate. At the edge of the viscous boundary layer (outside the thermal boundary layer) the horizontal component of the velocity is approximately equal to the wind $\widetilde{U}$, therefore the horizontal component of the velocity within the thermal boundary layer can be approximated as

$$\widetilde{u} = \frac{\widetilde{y}}{\widetilde{\delta}_u}\widetilde{U}.$$

Substituting the wind $\widetilde{U}$ (4.9) and the thickness of the viscous boundary layer (4.11) into this relation, one obtains the horizontal velocity within the thermal boundary layer:

$$\widetilde{u} = \frac{1}{C}\sqrt{\frac{\widetilde{U}_0^3(m+1)\widetilde{L}}{2\widetilde{\nu}}}\left(\frac{\widetilde{y}}{\widetilde{L}}\right)\left(\frac{\widetilde{x}}{\widetilde{L}}\right)^{(3m-1)/2}.$$

Because of the continuity equation, the vertical component of the velocity is equal to

$$\widetilde{v} = -\frac{3m-1}{4C}\sqrt{\frac{\widetilde{U}_0^3(m+1)\widetilde{L}}{2\widetilde{\nu}}}\left(\frac{\widetilde{y}}{\widetilde{L}}\right)^2\left(\frac{\widetilde{x}}{\widetilde{L}}\right)^{(3m-3)/2}.$$

Then in the considered case one obtains the following energy boundary layer equation:

$$\widetilde{u}\widetilde{T}_{\widetilde{x}} + \widetilde{v}\widetilde{T}_{\widetilde{y}} = \widetilde{\kappa}\widetilde{T}_{\widetilde{y}\widetilde{y}}. \tag{5.8}$$

Introducing the similarity variable ζ,

$$\zeta = \frac{1}{\Gamma(4/3)\,C^{1/3}}\left(\frac{\widetilde{U}_0(m+1)}{2\widetilde{L}^m}\right)^{1/2}\left(\frac{1}{6\widetilde{\kappa}}\right)^{1/3}\left(\frac{1}{\widetilde{\nu}}\right)^{1/6}\widetilde{y}\widetilde{x}^{(m-1)/2}, \tag{5.9}$$

where Γ is the gamma function, from (5.8) one obtains the following ordinary differential equation

$$\Theta_{\zeta\zeta} + 3\Gamma^3(4/3)\zeta^2\Theta_\zeta = 0 \tag{5.10}$$

for the dimensionless temperature Θ. This equation has a solution

$$\Theta(\zeta) = \int_0^\zeta \exp(-\Gamma^3(4/3)\chi^3)d\chi,$$

which satisfies the boundary conditions (5.6). This function is presented in figure 5 (b) with a continuous line.

From the definition of the similarity variable ζ (5.9) one further obtains

$$\widetilde{\delta}_\theta \sim \widetilde{\kappa}^{1/3}\widetilde{\nu}^{1/6}\sqrt{\frac{\widetilde{x}}{\widetilde{U}(x)}} = \sqrt{\frac{\widetilde{x}/\widetilde{L}}{Re}}\mathcal{P}r^{-1/3}\widetilde{L},$$

hence

$$\delta_\theta \equiv \frac{\widetilde{\delta}_\theta}{\widetilde{L}} \sim Re^{-1/2}\mathcal{P}r^{-1/3}\left(\frac{\widetilde{x}}{\widetilde{L}}\right)^{1/2} \tag{5.11}$$

with the local Reynolds number $Re = \widetilde{L}\widetilde{U}/\widetilde{\nu}$.

One can sum up the results (5.7) and (5.11) as follows: for very small and very large

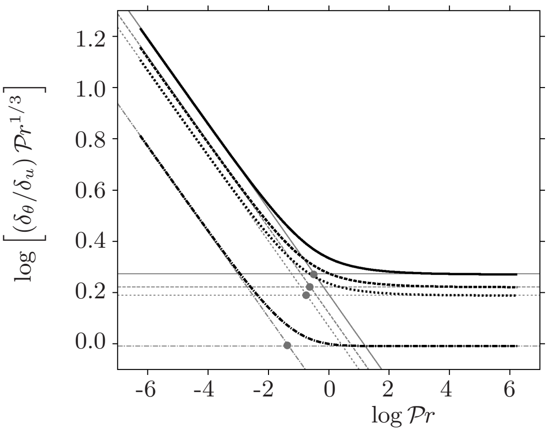

FIGURE 7. The dependency of the ratio δ_θ/δ_u of the thermal and viscous boundary layer thicknesses on Prandtl number for $m = 0$ (Prandtl–Blasius flow, -·-), $m = 1/3$ (···), $m = 1/2$ (- -) and $m = 1$ (stagnation-point flow, —). Critical Prandtl number $\mathcal{P}r^* \approx 0.27m + 0.05$ (grey dots) for the regime change of δ_θ/δ_u from $\sim \mathcal{P}r^{-1/2}$ to $\sim \mathcal{P}r^{-1/3}$.

Prandtl numbers the thickness of the thermal boundary layer scales as

$$\delta_\theta \equiv \frac{\widetilde{\delta}_\theta}{\widetilde{L}} \sim \begin{cases} Re^{-1/2}\mathcal{P}r^{-1/2}\left(\widetilde{x}/\widetilde{L}\right)^{1/2}, & \mathcal{P}r \ll 1, \\ Re^{-1/2}\mathcal{P}r^{-1/3}\left(\widetilde{x}/\widetilde{L}\right)^{1/2}, & \mathcal{P}r \gg 1. \end{cases}$$

Since the thickness of the viscous boundary layer scales as in (4.12) and is independent from Prandtl number, the ratio of the thermal and viscous boundary layers scales with the Prandtl-number as follows:

$$\delta_\theta/\delta_u \sim \begin{cases} \mathcal{P}r^{-1/2}, & \mathcal{P}r \ll 1, \\ \mathcal{P}r^{-1/3}, & \mathcal{P}r \gg 1, \end{cases} \tag{5.12}$$

for all possible m. This means that the ratio δ_θ/δ_u is independent from the Reynolds number as well as from the horizontal coordinate $\widetilde{x}$.

6. Ratio of the thermal and viscous boundary layers

One can solve numerically the system (5.1), (5.2) for all possible values of m and $\mathcal{P}r$ and then evaluate the thicknesses of the viscous ($\widetilde{\delta}_u$) and thermal ($\widetilde{\delta}_\theta$) boundary layers, based on the slope method. The ratio of the thicknesses with respect to the similarity variable ξ is equal the ratio of the thicknesses in the physical space (Shishkina *et al.* 2010).

In figure 7 the dependency of the ratio δ_θ/δ_u, normalised with $\mathcal{P}r^{-1/3}$, is presented for some particular values of m. As it was already derived in the previous section, for all m, the ratio scales as $\sim \mathcal{P}r^{-1/2}$ for small and as $\sim \mathcal{P}r^{-1/3}$ for large Prandtl numbers. For the Prandtl–Blasius flow ($m = 0$), the ratio can be approximated as

$$\left.\frac{\delta_\theta}{\delta_u}\right|_{m=0} \approx \begin{cases} 0.589\mathcal{P}r^{-1/2}, & \mathcal{P}r < 3\times10^{-4}, \\ \mathcal{P}r^{-0.357+0.022\log\mathcal{P}r}, & 3\times10^{-4} \leqslant \mathcal{P}r \leqslant 3, \\ 0.982\,\mathcal{P}r^{-1/3}, & 3 < \mathcal{P}r, \end{cases} \tag{6.1}$$

as it was shown in Shishkina *et al.* (2010). Here and further $\log \equiv \log_{10}$ is the logarithm to base 10. For $m = 1/3$, $m = 1/2$ and $m = 1$ (stagnation-point flow) one can take, respectively, the following approximations:

$$\left.\frac{\delta_\theta}{\delta_u}\right|_{m=1/3} \approx \begin{cases} 1.170\mathcal{P}r^{-1/2}, & \mathcal{P}r < 10^{-3}, \\ 1.736\mathcal{P}r^{-0.393+0.017\log\mathcal{P}r}, & 10^{-3} \leqslant \mathcal{P}r \leqslant 10^{2}, \\ 1.550\,\mathcal{P}r^{-1/3}, & 10^{2} < \mathcal{P}r, \end{cases} \tag{6.2}$$

$$\left.\frac{\delta_\theta}{\delta_u}\right|_{m=1/2} \approx \begin{cases} 1.318\mathcal{P}r^{-1/2}, & \mathcal{P}r < 10^{-3}, \\ 1.902\mathcal{P}r^{-0.395+0.017\log\mathcal{P}r}, & 10^{-3} \leqslant \mathcal{P}r \leqslant 10^{2}, \\ 1.675\,\mathcal{P}r^{-1/3}, & 10^{2} < \mathcal{P}r, \end{cases} \tag{6.3}$$

and

$$\left.\frac{\delta_\theta}{\delta_u}\right|_{m=1} \approx \begin{cases} 1.561\mathcal{P}r^{-1/2}, & \mathcal{P}r < 10^{-3}, \\ 2.183\mathcal{P}r^{-0.400+0.017\log\mathcal{P}r}, & 10^{-3} \leqslant \mathcal{P}r \leqslant 10^{3}, \\ 1.879\,\mathcal{P}r^{-1/3}, & 10^{3} < \mathcal{P}r. \end{cases} \tag{6.4}$$

Figure 7 reveals that for a fixed $\mathcal{P}r$ the ratio δ_θ/δ_u is larger for larger m. Let $\mathcal{P}r^*$ be the critical Prandtl number, i.e. that Prandtl number at which the asymptotes for the regimes $\sim \mathcal{P}r^{-1/2}$ for small $\mathcal{P}r$ and $\sim \mathcal{P}r^{-1/3}$ for large $\mathcal{P}r$ intersect. The numerically evaluated approximation of the critical Prandtl numbers $\mathcal{P}r^*$, which are marked in figure 7 with grey dots, is the following:

$$\mathcal{P}r^* \approx 0.27m + 0.05. \tag{6.5}$$

Thus, one obtains $\mathcal{P}r^* \approx 0.046$ for $m = 0$, $\mathcal{P}r^* \approx 0.185$ for $m = 1/3$, $\mathcal{P}r^* \approx 0.229$ for $m = 1/2$ and $\mathcal{P}r^* \approx 0.325$ for $m = 1$.

It is well-known that in the case of Prandtl–Blasius flow ($m = 0$) the viscous and the thermal boundary layers have the same thickness for $\mathcal{P}r = 1$. For larger m the Prandtl number should be also larger in order to provide equal thicknesses of the boundary layers. In particular, from (6.2), (6.3) and (6.4) one obtains that $\delta_\theta/\delta_u = 1$ for $\mathcal{P}r = 4.24$ if $m = 1/3$, for $\mathcal{P}r = 5.35$ if $m = 1/2$ or for $\mathcal{P}r = 7.59$ if $m = 1$.

For the operating fluids air ($\mathcal{P}r = 0.786$) and water ($\mathcal{P}r = 4.38$), which we study in our DNS of turbulent RBC, from (6.1), (6.2), (6.3) and (6.4) one obtains the following estimations of the ratio of the thermal and viscous boundary layer thicknesses, dependently on the pitch angle β of the wind:

$$\left.\frac{\delta_\theta}{\delta_u}\right|_{\mathcal{P}r=0.786} \approx \begin{cases} 1.08, & \beta = \pi \quad (m = 0), \\ 1.88, & \beta = 3\pi/4 \quad (m = 1/3), \\ 2.06, & \beta = 2\pi/3 \quad (m = 1/2), \\ 2.37, & \beta = \pi/2 \quad (m = 1), \end{cases} \tag{6.6}$$

and

$$\left.\frac{\delta_\theta}{\delta_u}\right|_{\mathcal{P}r=4.38} \approx \begin{cases} 0.60, & \beta = \pi \quad (m = 0), \\ 0.98, & \beta = 3\pi/4 \quad (m = 1/3), \\ 1.07, & \beta = 2\pi/3 \quad (m = 1/2), \\ 1.23, & \beta = \pi/2 \quad (m = 1), \end{cases} \tag{6.7}$$

respectively.

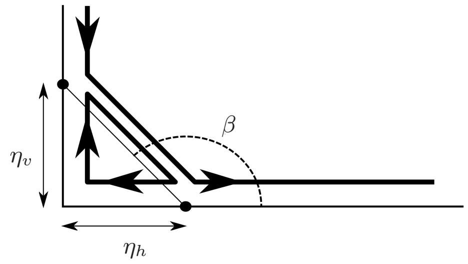

FIGURE 8. Sketch of the large-scale circulation (wind) and secondary roll within the plane of the large-scale circulation. Dots mark the locations, where the wall shear stress is equal to zero. The distances from the left bottom corner to the these locations are denoted as η_v and η_h. The angle β, at which the wind attacks the horizontal plate, is determined by (7.1).

7. Theory versus the DNS results

The value of m and the thicknesses of the thermal ($\widetilde{\delta}_\theta$) and viscous ($\widetilde{\delta}_u$) boundary layers are extracted from our DNS as follows. First, the temperature distributions on the vertical wall are used to determine the instantaneous orientation of the LSC in a similar way as it was done by Brown & Ahlers (2006) and Wagner *et al.* (2012). Further, time periods without serious reorientations of the LSC are detected, which last up to 682 time units. Note that each time unit equals $(\widetilde{H}/(2\widetilde{\alpha}\widetilde{g}\widetilde{\Delta}))^{1/2}$. During these periods the angle corresponding to the LSC plane does not change more than 0.06π. In the conducted analysis of the DNS data the mean orientation during this time periods is chosen to fix the LSC plane (cf. figure 2, left). Within this plane the instantaneous flow fields, which are recorded with a sampling rate of three per time unit, are analysed and the local instantaneous thicknesses of the viscous and thermal boundary layers close to the heated bottom plate are determined by applying the slope method, in a similar way as it is done in the above theory.

In order to estimate the angle β, at which the large-scale circulation attacks the heated/cooled plates, we first find locations within the plane of the large-scale circulation, where the time-averaged wall shear stress is equal to zero. Here η_h and η_v are the distances from the left bottom corner to the next locations at, respectively, the bottom or left vertical wall, where the wall shear stress τ_w is equal to zero (see a sketch in figure 8). The values of β and m can be then estimated as follows:

$$\beta = \pi - \arctan(\eta_v/\eta_h), \tag{7.1}$$
$$m = \pi/\beta - 1. \tag{7.2}$$

In figure 9 the time-averaged wall shear stresses at the bottom and left vertical wall from figure 8 in the plane of the large-scale circulation are presented for water and air and different Rayleigh numbers. On can see that locations η_v and η_h depend only weakly (and nonmonotonically) on the Rayleigh number and Prandtl number, at least for the considered diapason of $\mathcal{R}a$ and $\mathcal{P}r$. Thus, for the operating fluids air and water we obtained

$$\beta = \begin{cases} 0.695\pi \pm 0.015\pi & \text{(air)}, \\ 0.705\pi \pm 0.025\pi & \text{(water)}; \end{cases} \tag{7.3}$$

$$m = \begin{cases} 0.44 \pm 0.02 & \text{(air)}, \\ 0.42 \pm 0.05 & \text{(water)}. \end{cases} \tag{7.4}$$

In figure 10 the ratios $\langle \delta_\theta/\delta_u \rangle_t$ of the thermal and viscous boundary layer thicknesses

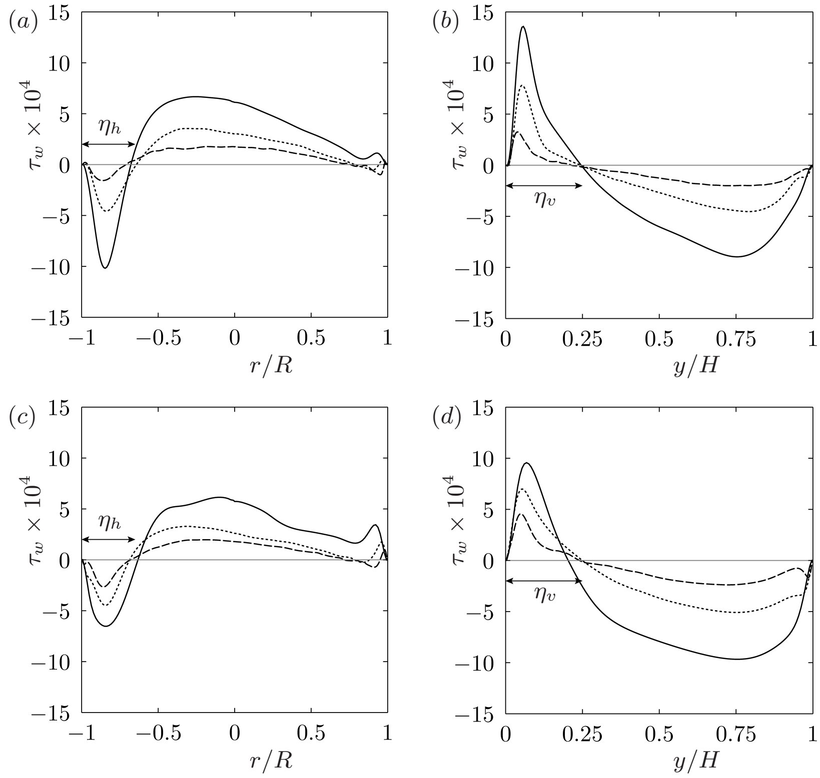

FIGURE 9. Time-averaged wall shear stress at the bottom plate (a, c) and left vertical wall (b, d) in the plane of the large-scale circulation, as obtained in the DNS for air (a, b) and water (c, d), for $\mathcal{R}a = 10^7$ (——), $\mathcal{R}a = 10^8$ $(\cdots)$ and $\mathcal{R}a = 10^9$ (- - -) with the distances η_v and η_h, as in figure 8.

are presented in dependence of the radial position r (see figure 2, left), as they were obtained in the DNS of turbulent RBC of air and water for different Rayleigh numbers, together with their theoretical estimates (6.6) and (6.7). Here $\langle \cdots \rangle_t$ denotes the time averaging. The lowest and the highest horizontal dash-lines in figures 10 (a) and 10 (b) represent the estimations (6.6), (6.7) for $m = 0$ (Prandtl–Blasius flow) and $m = 1$ (stagnation-point flow), respectively.

As one can see in figure 10, the ratio of the time-averaged thicknesses of the thermal and viscous boundary layers remains almost constant along the path of the wind (apart from the secondary rolls) and depends only weakly on the Rayleigh number. Since the wind is a non-horizontal flow and the angle β between its direction and the horizontal plate belongs to the interval $[\frac{\pi}{2}, \frac{3\pi}{4}]$, the predictions of the ratios δ_θ/δ_u with the approximations (6.6) and (6.7) for $m \in [1/3; 1]$ are found to be more reliable than those for $m = 0$ (Prandtl–Blasius flow).

For higher Rayleigh numbers the difference between $\langle \delta_\theta/\delta_u \rangle_t$, evaluated from the DNS data, and the above described Falkner–Skan approximation of $\langle \delta_\theta/\delta_u \rangle_t$ for the Rayleigh–Bénard boundary layers becomes more visible, which is explained by the increasing influence of the fluctuations in the boundary layers and, hence, a stronger deviation of the real flows from this stationary 2D model. Another observation is that for smaller Prandtl numbers the Falkner–Skan approximation provides more accurate predictions compared

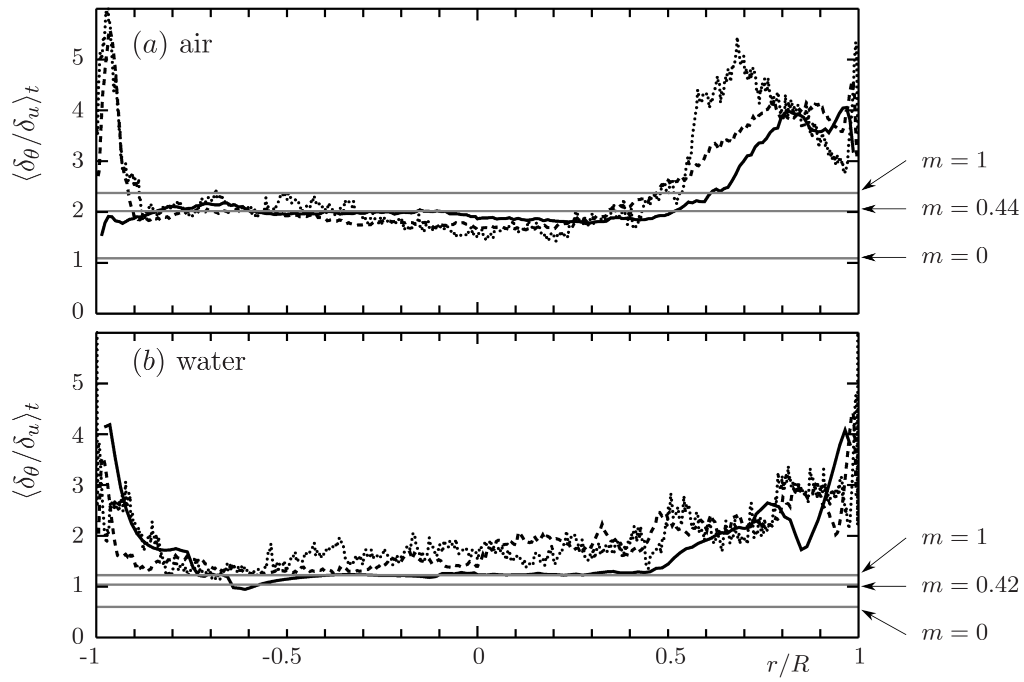

FIGURE 10. Ratio $\langle \delta_\theta/\delta_u \rangle_t$ of the thermal and viscous boundary layer thicknesses for (a) air, $\mathcal{P}r = 0.786$, and (b) water, $\mathcal{P}r = 4.38$, as obtained in DNS for $\mathcal{R}a = 10^9$ ($\cdots$), $\mathcal{R}a = 10^8$ (- - -), $\mathcal{R}a = 10^7$ (—) together with the theoretical predictions for $m = 0$ (Prandtl–Blasius flow), $m = 1$ (stagnation-point flow) and $m = 0.44$ (a) and $m = 0.42$ (b), as estimated from the DNS data, according to (7.1), (7.2), (7.4).

to the large-Prandtl-number case, in which, in particular, for very large $\mathcal{P}r$ the existence of the wind itself become questionable (Schmalzl *et al.* 2004; Horn *et al.* 2013).

8. Conclusions

The non-zero pressure gradient in the Rayleigh–Bénard convection cell influences the velocity of the large-scale circulation and all boundary layer characteristics. Therefore in the present work we considered a system of the boundary layer momentum and energy equations (3.5)-(3.7), which takes into account the presence of the non-zero pressure gradient. It was shown, that for the existence of the similarity solution of the this system an exponential (4.3) or a power-function (4.9) wind above the viscous boundary layer is required.

The power-function wind (4.9), in contrast to the exponential one (4.3), leads to a simultaneous increase of the thickness of the viscous boundary layers and the magnitude of the LSC along its path, what is very similar to the situation that we observed in our DNS. Therefore the case of the power-function wind was investigated in detail, which lead to the Falkner–Skan boundary layer equations (5.1), (5.2) to describe the Rayleigh–Bénard boundary layers. These equations and their similarity solutions depend not only on the Prandtl number, but also on the angle β (4.15), at which the large-scale circulation (see figure 8) attacks the horizontal plate.

For the normalised temperature profiles, which satisfy (5.6) and can be obtained under the assumption of a power-function wind above the viscous boundary layer, a general result was derived. For all angles β and all Prandtl numbers, the temperature profiles are bounded by $\Theta(\zeta) = \int_0^\zeta \exp(-B\chi^\omega)\,\mathrm{d}\chi$ with $B = \begin{cases} \Gamma^3(4/3) \approx 0.712, & \omega = 3, \; \mathcal{P}r \gg 1, \\ \pi/4, & \omega = 2, \; \mathcal{P}r \ll 1. \end{cases}$ This limits are also valid for the particular case of Prandtl–Blasius boundary layers.

For the ratio of the thermal and viscous boundary layer thicknesses it was derived that for all β it scales as $\delta_\theta/\delta_u \sim \mathcal{P}r^{-1/2}$ if $\mathcal{P}r \ll 1$ and $\delta_\theta/\delta_u \sim \mathcal{P}r^{-1/3}$ if $\mathcal{P}r \gg 1$. The asymptotes for these regimes intersect at the critical Prandtl number $\mathcal{P}r^*$, which grows together with decreasing β and can be approximated by (6.5). For certain particular angles β of the wind attack, formulae (6.1)–(6.4) to approximate δ_θ/δ_u as functions on $\mathcal{P}r$ were derived based on the numerical solutions of the boundary layer equations.

Using our DNS data for air and water we estimated the angle β, based on the information of the locations within the plane of the large-scale circulation, where the time-averaged wall shear stress vanishes. Thus it was obtained that $\beta = 0.695\pi \pm 0.015\pi$ for air and $\beta = 0.705\pi \pm 0.025\pi$ for water. The theoretical predictions obtained in the present work demonstrated a good agreement with the DNS results for turbulent RBC with the considered Rayleigh and Prandtl numbers.

From the fact that the Falkner–Skan ansatz for $\beta \neq \pi$ represents the DNS data in a better way than the Prandtl–Blasius one for $\beta = \pi$, one concludes that the angle β of the wind attack may also influence the constants in the scaling laws of the Reynolds and Nusselt numbers with the Rayleigh and Prandtl numbers in turbulent RBC with laminar-like boundary layers. In this case a parameter like m, which determines the angle β (4.15) and influences the pressure gradient within the viscous boundary layer and the wind (4.9) above the boundary layer, will be involved in the scaling theory, representing the details on the global flow structure.

Further, since the geometry of the container influences the global flow structure and, hence, the angle β at which the wind meets the boundary layer, the Falkner-Skan approximation will lead to an improvement of the models that account for the influence of the regular wall roughness and isothermal obstacles inside the convection cells (Shishkina & Wagner 2011). The Falkner–Skan ansatz will be also useful for a better understanding of mixed convection flows (Bailon-Cuba *et al.* 2012; Shishkina & Wagner 2012), which are even more sensitive to the angle of the wind attack, and especially of forced convection flows (Koerner *et al.* 2013) that are driven by imposed pressure gradients. These and many other issues related to the applicability of the Falkner–Skan ansatz in turbulent thermal convection should be investigated in the future.

The authors are grateful to Professor S. Grossmann and all participants of the International Conference on Rayleigh–Bénard Turbulence, held in December 2012 in Hong Kong, for very useful discussions on different aspects concerning this work. The authors also acknowledge financial support of the Deutsche Forschungsgemeinschaft (DFG) under the grants SH405/2-1 and SH405/3-1.

REFERENCES

Ahlers, G., Bodenschatz, E., Funfschilling, D., Grossmann, S., X.He, Lohse, D., Stevens, R.J.A.M. & Verzicco, R. 2012 Logarithmic temperature profiles in turbulent Rayleigh-Bénard convection. *Phys. Rev. Lett.* **109**, 114501.

Ahlers, G., Grossmann, S. & Lohse, D. 2009 Heat transfer and large scale dynamics in turbulent Rayleigh-Bénard convection. *Rev. Mod. Phys.* **82**, 503–537.

Bailon-Cuba, J., Shishkina, O., Wagner, C. & Schumacher, J. 2012 Low-dimensional model of turbulent mixed convection in a complex domain. *Phys. Fluids* **24**, 107101.

Blasius, H. 1908 Grenzschichten in Flüssigkeiten mit kleiner Reibung. *Z. Math. Phys.* **56**, 1–37.

Brown, E. & Ahlers, G. 2006 Rotations and cessations of the large-scale circulation in turbulent Rayleigh-Bénard convection. *J. Fluid Mech.* **568**, 351–386.

Calzavarini, E., Doering, C. R., Gibbon, J. D., Lohse, D., Tanabe, A. & Toschi, F. 2006 Exponentially growing solutions in homogeneous Rayleigh–Bénard convection. *Phys. Review E* **73**, 035301.

Chillà, F. & Schumacher, J. 2012 New perspectives in turbulent Rayleigh-Bénard convection. *Eur. Phys. J. E* **35**, 58.

Ching, E. S. C. 1997 Heat flux and shear rate in turbulent convection. *Phys. Rev. E* **55**, 1189–1192.

Falkner, V. M. & Skan, S. W. 1931 Some approximate solutions of the boundary layer equations. *Phyl. Mag.* **12**, 865–896.

Funfschilling, D. & Ahlers, G. 2004 Plume motion and large-scale dynamics in a cylindrical Rayleigh–Bénard cell. *Phy. Rev. Lett.* **92**, 194502.

Gauthier, F. & Roche, P.-E. 2008 Evidence of a boundary layer instability at very high Rayleigh number. *Europhys. Lett.* **83**, 24005.

Grossmann, S. & Lohse, D. 2000 Scaling in thermal convection: A unifying view. *J. Fluid Mech.* **407**, 27–56.

Grossmann, S. & Lohse, D. 2001 Thermal convection for large Prandtl numbers. *Phys. Rev. Lett.* **86**, 3316–3319.

Grossmann, S. & Lohse, D. 2011 Multiple scaling in the ultimate regime of thermal convection. *Phys. Fluids* **23**, 045108.

Grossmann, S. & Lohse, D. 2012 Logarithmic temperature profiles in the ultimate regime of thermal convection. *Phys. Fluids* **24**, 125103.

Horn, S., Shishkina, O. & Wagner, C. 2011 The influence of non-Oberbeck-Boussinesq effects on rotating turbulent Rayleigh–Bénard convection. *J. Phys.: Conf. Ser.* **318**, 082005.

Horn, S., Shishkina, O. & Wagner, C. 2013 On non-Oberbeck-Boussinesq effects in three-dimensional Rayleigh-Bénard convection in glycerol. *J. Fluid Mech.* **724**, 175–202.

Kaczorowski, M., Shishkina, O., Shishkin, A., Wagner, C. & Xia, K.-Q. 2011 Analysis of the large-scale circulation and the boundary layers in turbulent Rayleigh–Bénard convection. In *Direct and Large-Eddy Simulation VIII* (ed. H. Kuerten, B. Geurts, V. Armenio & J. Fröhlich), pp. 383–388. Springer.

Koerner, M., Shishkina, O., Wagner, C. & Thess, A. 2013 Properties of large-scale flow structures in an isothermal ventilated room. *Building and Environment* **59**, 563–574.

Lohse, D. & Xia, K.-Q. 2010 Small-scale properties of turbulent Rayleigh-Bénard convection. *Annu. Rev. Fluid Mech.* **42**, 335–364.

Pohlhausen, K. 1921 Zur nährungsweisen Integration der Differentialgleichung der laminaren Grenzschicht. *Z. Angew. Math. Mech.* **1**, 252–268.

Prandtl, L. 1905 Über Flüssigkeitsbewegung bei sehr kleiner Reibung. In *Verhandlungen des III. Int. Math. Kongr., Heidelberg, 1904*, pp. 484–491. Leipzig: Teubner.

du Puits, R., Resagk, C., Tilgner, A., Busse, F. H. & Thess, A. 2007 Structure of thermal boundary layers in turbulent Rayleigh-Bénard convection. *J. Fluid Mech.* **572**, 231–254.

Scheel, J. D., Kim, E. & White, K. R. 2012 Thermal and viscous boundary layers in turbulent Rayleigh-Bénard convection. *J. Fluid Mech.* **711**, 281–305.

Schlichting, H. & Gersten, K. 2000 *Boundary-Layer Theory*, 8th edn. Springer.

Schmalzl, J., Breuer, M. & Hansen, U. 2004 On the validity of two-dimensional numerical approaches to time-dependend thermal convection. *Europhys. Lett.* **67**, 390–396.

Shi, N., Emran, M. S. & Schumacher, J 2012 Boundary layer structure in turbulent Rayleigh-Bénard convection. *J. Fluid Mech.* **706**, 5–33.

Shishkina, O., Stevens, R. J. A. M., Grossmann, S. & Lohse, D. 2010 Boundary layer structure in turbulent thermal convection and its consequences for the required numerical resolution. *New J. Phys.* **12**, 075022.

Shishkina, O. & Thess, A. 2009 Mean temperature profiles in turbulent Rayleigh-Bénard convection of water. *J. Fluid Mech.* **663**, 449–460.

Shishkina, O. & Wagner, C. 2005 A fourth order accurate finite volume scheme for numerical simulations of turbulent Rayleigh-Bénard convection in cylindrical containers. *C. R. Mecanique* **333**, 17–28.

Shishkina, O. & Wagner, C. 2011 Modelling the influence of wall roughness on heat transfer in thermal convection. *J. Fluid Mech.* **686**, 568–582.

Shishkina, O. & Wagner, C. 2012 A numerical study of turbulent mixed convection in an enclosure with heated rectangular elements. *J. Turbulence* **13**, 1–21.

Siggia, E. 1994 High Rayleigh number convection. *Annu. Rev. Fluid Mech.* **26**, 137–168.

Stevens, R. J. A. M., van der Poel, E. P., Grossmann, S. & Lohse, D. 2013 The unifying theory of scaling in thermal convection: The updated prefactors. *J. Fluid Mech.* **submitted**.

Stevens, R. J. A. M., Verzicco, R. & Lohse, D. 2010 Radial boundary layer structure and Nusselt number in turbulent Rayleigh–Bénard convection. *J. Fluid Mech.* **643**, 495–507.

Stevens, R. J. A. M., Zhou, Q., Grossmann, S., Verzicco, R., Xia, K.-Q. & Lohse, D. 2012 Thermal boundary layer profiles in turbulent Rayleigh–Bénard convection in a cylindrical sample. *Phys. Rev. E* **85**, 027301.

Stewartson, K. 1958 On the free convection from a horizontal plate. *Z. angew. Math. Phys.* **9a**, 276–282.

Sun, C., Cheung, Y.-H. & Xia, K.-Q. 2008 Experimental studies of the viscous boundary layer properties in turbulent Rayleigh-Bénard convection. *J. Fluid Mech.* **605**, 79–113.

Tilgner, A., Belmonte, A. & Libchaber, A. 1993 Temperature and velocity profiles of turbulent convection in water. *Phys. Rev. E* **47**, 2253–2257.

Verzicco, R. 2012 Boundary layer structure in confined turbulent thermal convection. *J. Fluid Mech.* **706**, 1–4.

Wagner, S., Shishkina, O. & Wagner, C. 2012 Boundary layers and wind in cylindrical Rayleigh–Bénard cells. *J. Fluid Mech.* **697**, 336–366.

Weiss, S. & Ahlers, G. 2011 The large-scale flow structure in turbulent rotating Rayleigh–Bénard convection. *J. Fluid Mech.* **688**, 461–492.

Wilcox, D. C. 2010 *Basic Fluid Mechanics*, 4th edn. DCW Industries.

Xi, H.-D. & Xia, K.-Q. 2007 Cessations and reversals of the large-scale circulation in turbulent thermal convection. *Phys. Rev. E* **76**, 036301.

Xia, K.-Q. 2011 How heat transfer efficiencies in turbulent thermal convection depend on internal flow modes. *J. Fluid Mech.* **676**, 1–4.

Zhou, Q. & Xia, K.-Q. 2010 Measured instantaneous viscous boundary layer in turbulent Rayleigh-Bénard convection. *Phys. Rev. Lett.* **104**, 104301.